Effects of the promotion with bismuth and lead on direct synthesis of light olefins from syngas over carbon nanotube supported iron catalysts

Bang Gu[a], Vitaly V. Ordomsky[a,*], Mounib Bahri[b], Ovidiu Ersen[b], Petr A. Chernavskii[c], Dmitry Filimonov[c], Andrei Y. Khodakov[a,*]

[a] Univ. Lille, CNRS, Centrale Lille, ENSCL, Univ. Artois, UMR 8181 – UCCS – Unité de Catalyse et Chimie du Solide, F-59000 Lille, France
[b] IPCMS-UMR 7504 CNRS, Université de Strasbourg, 23 rue du Loess, BP 43-67034 Strasbourg Cedex 2, France
[c] Department of Chemistry, Moscow State University, 119992 Moscow, Russia

ABSTRACT

Light olefins are important platform molecules in chemical industry. Fischer-Tropsch synthesis provides an alternative technology for direct synthesis of light olefins from syngas, which can be generated from renewable feedstocks such as organic waste, used plastics and biomass. The Bi- and Pb-promoted iron catalysts supported by carbon nanotubes have been prepared for direct conversion of syngas to lower olefins. Compared to the unpromoted iron catalysts, a twice higher Fischer-Tropsch reaction rate and higher selectivity to lower olefins were obtained. A combination of characterization techniques reveals remarkable migration the promoting elements, which occurs during the catalyst activation. After the activation, the iron carbide nanoparticles are decorated with the promoting elements. The lower melting points and high mobility of these two metal promoters during the catalyst activation are crucial for the intimate contact between Fe and promoters. The promoting effects of bismuth and lead result in a better reducibility and easier carbidisation of iron nanoparticles. The higher yield of light olefins over the carbon nanotube supported catalysts in the presence of promoters is due to slowing down secondary hydrogenation of olefins and a decrease in the chain growth probability.

1. Introduction

Development of novel routes for the efficient utilization of non-petroleum resources including organic waste, used plastics and biomass to produce chemicals and ultraclean liquid fuels has attracted much attention because of environmental concerns and the depletion of fossil resources. Lower olefins (C_2-$C_4^=$) are key building blocks in the chemical industry. They are important intermediates for production of a wide range of packing materials, synthetic textiles and solvents [1,2].

In conventional technologies, light olefins are produced from steam cracking of naphtha, ethane cracking, methanol to olefins (MTO) and dimethyl ether to olefins (DMTO) processes. In the naphtha steam cracking, olefins are by-products and the selectivity to specific olefins is low. Ethylene is also produced by cracking of ethane present in the shale gas. Despite many important advantages, this process however requires very high temperature and yields only ethylene. The MTO and DMTO processes have been developed and commercialized in several countries with important coal resources [3–5]. MTO and DMTO show high selectivity towards lower olefins, while the technologies are multistage and require synthesis of intermediate products such as

methanol and dimethyl ether. Catalyst deactivation has been a serious challenge of these processes.

Recently, two groups in China reported the new OX-ZEO process, which is based on the combination of methanol synthesis and MTO on a single bifunctional catalyst constituted either by the Zn-Cr [6] or by Zr-Zn [7] systems and SAPO-34. It is important to emphasize that different to FT synthesis, the selectivity of the OX-ZEO process can be potentially higher than that of the conventional FT synthesis. In the conventional FT synthesis, the maximum selectivity to the C_2-C_4 hydrocarbons (including both olefins and paraffins) is around 58% with the chain growth probability (α) of 0.46. The challenges of this new technology are relevant to attaining higher olefin yields and improving catalyst stability at higher CO conversion levels [8].

Fischer-Tropsch to Olefins (FTO) is a key process for the direct single-step transformation of various alternative carbon resources such as coal, natural gas, renewable biomass and waste into lower olefins via syngas [9–11]. Iron-based catalysts are the catalysts of choice for the FTO process because of their high selectivity towards lower olefins, lower cost and high water-gas-shift activity, which can adjust the H_2/CO ratio in syngas produced from the biomass- or coal-derived

feedstocks [12,13]. Iron has also stronger resistance to the contaminants in syngas (sulfur, nitrogen compounds) compared with cobalt and ruthenium based catalysts.

The iron-based catalysts for FT synthesis can be divided into two major groups: bulk catalysts and supported catalysts. Although the unsupported fused or precipitated iron catalysts modified by promoters can achieve high selectivity to lower olefins, their poor mechanical stability especially in the presence of carbidisation/decarbidisation results in breaking up of the iron particles, formation of fines and thus, can be prohibitive for the practical applications [14].

Porous supports with high surface area are favorable for better dispersion of iron active phase and therefore for enhanced catalytic performance. Catalytic supports can be also efficient in increasing the mechanical stability of iron-based catalysts. Several supports (oxide, zeolites, carbon materials) have been used for iron FT catalysts.

The properties of the FT catalysts can be modified by adding electronic or structural promoters to improve the selectivity to light olefins or to enhance catalytic activity [15,16]. Among various promoters, potassium [17,18], sodium [19,20,21], copper [22], manganese [23] and zinc [21] are often used. These promoters are considered to work as electronic donors, which tune the CO and H_2 chemisorption and dissociation on the catalyst surfaces. Consequently, the reaction selectivity to lower olefins could be significantly improved. Several authors also consider Ln and Zn as structural promoters. Lohitharn [24,25] et al investigated the silica supported iron catalysts promoted with Mn and identified the role of Mn as a structural promoter. Higher reaction rates observed for the Mn-promoted Fe catalysts were attributed to higher number of active surface intermediates, while their intrinsic activity was not affected. Ma et al. [21] considered Zn as a structural promoter in their catalysts.

De Jong and co-workers [14] observed enhanced selectivity to light olefins (about 60%) over a modified Fe/α-Al_2O_3 catalyst containing small amounts of sulfur and sodium. The best results in that report were obtained at very low CO conversion. The inert α-Al_2O_3 support showed week interaction with iron species. It was suggested that sodium could reduce methane selectivity by increasing the chain growth probability while sulfur have reduced the hydrogen coverage of the catalyst and its hydrogenation activity. The proximity between iron and promoters (Na, S) was a key parameter, which determined hydrocarbon distribution [26,27]. Recently we observed [28] a remarkable increase in the FT reaction rate and light olefin selectivities over the silica supported iron catalysts promoted with soldering elements such as Bi and Pb.

It is known that the catalyst structure can significantly evolve during many catalytic reactions. The active phase can be modified and promoters can migrate to or from the active sites [29,30]. Li et al. [31] found that Mn could migrate to the surface of the iron and result in encapsulation of unreduced FeO in MnO. The migration of the alkali promoters from iron catalysts may cause deterioration of the support acidity and then increase carbon deposition. The migration of promoters may also have an effect on the product selectivity. As a result, the reaction shifts towards lighter and more paraffinic hydrocarbons, which are usually observed over the unpromoted catalysts [32].

Carbon nanotubes (CNT) as catalytic supports for iron Fischer-Tropsch catalysts have several important advantages. Different to commonly used oxide supports, carbon does not form inert mixed compounds between iron and supports (e.g. iron silicate or aluminate) which are difficult to reduce and to carbidize during the catalyst activation and reaction. Iron catalysts supported on carbon nanotubes and activated carbon show highest activity in FT synthesis, which could be attributed to the formation of composites of iron carbide and residual magnetite [19] and to possible electronic transfer between carbon and iron species [33].

Similar to metal oxide-supported catalysts, Fe catalysts supported on carbon materials are sensitive to promoters, especially alkali metals. Xu et al. [34] reported that on the CNT-supported Fe-Mn nanoparticles, the selectivity to lower olefins was 31.5% with the methane selectivity

of 6.1%. However the CO conversion decreased from 60.2% to 43.9% after adding the Mn elements. Lu et al. [35] found that iron catalysts decorated with K and supported on N-CNT showed increase in lower olefin selectivity (54.6%), compared to the Fe/N-CNT catalyst. The iron catalysts supported by CNT and promoted with Mo also showed an increase in the selectivity to lower olefins from 30% to 40%, while the reaction rate was not much affected [36]. Finally, more accurate information about localization of iron and promoters can be obtained on the catalysts supported by CNT, because of better contrast in TEM and other imaging techniques.

The present paper focuses on the promotion of carbon nanotube supported iron catalysts with Bi and Pb for direct light olefin synthesis. This paper has two specific objectives: first, to develop extremely active and selective iron catalysts for direct olefin synthesis on the basis of CNT; second, to provide deep insights into the localization and structure of active sites and mechanisms of interaction of the Bi and Pb promoters with iron carbide and CNT. At different stages of catalyst preparation, activation and catalytic reaction, the catalysts were characterized by combination of techniques; the catalytic performance was evaluated in a fixed bed reactor at a wide range of operating conditions.

2. Experimental

2.1. Catalyst preparation

Prior to the impregnation, the multi-walled carbon nanotubes (CNT, Iolitec nanomaterial, 95%, outer diameter of 20–40 nm) were treated with nitric acid to remove contaminations with metals and to make CNT hydrophilic. The hydrophilicity of CNTs obtained after the treatment in nitric acid makes it easier for impregnation with aqueous solutions. The oxygen-containing groups also help to anchor the cations in the surface of CNTs and then to reduce sintering during the calcination. Typically, 3 g of CNT were pretreated in concentrated HNO_3 (68%, 210 mL) during 14 h under reflux conditions at 140 °C. After, the samples were filtered, washed with distilled water until pH = 7 and dried at 100 °C overnight. The iron catalysts were prepared by incipient wetness impregnation of CNT support with aqueous solutions of iron nitrate (Fe $(NO_3)_3$·$9H_2O$, Sigma-Aldrich). Lead nitrate (Pb$(NO_3)_2$, Sigma-Aldrich) and bismuth nitrate (Bi$(NO_3)_3$·$5H_2O$, Sigma-Aldrich) were used for preparation of the Bi- and Pb-promoted iron catalysts by co-impregnation. The Fe loading was fixed at 10 wt.%. The molar ratios of Fe/Pb and Fe/Bi are 100/2. The Bi/CNT (10 wt. %) and Pb/CNT (10 wt. %) catalysts were prepared by impregnation of CNT with bismuth and lead nitrates. After the impregnation, the samples were dried in an oven at 80 °C for 12 h followed by thermal treatment at 400 °C for 4 h under a flow of nitrogen (50 mL/min). The calcined catalysts are labeled as FeM /CNT, where M represents the promoters (Bi or Pb).

For comparison, several Bi- and Pb-promoted iron catalysts were prepared by mechanical mixing. The Fe/CNT and Bi/CNT or Pb/CNT samples were mechanically mixed in an agate mortar for 10 min to attain the same molar ratio. The obtained physical mixtures were denoted as Fe/CNT + M/CNT, where M represents the promoters (Bi or Pb).

2.2. Catalyst characterization

N_2 physisorption measurements were carried out using a Micromeritics Tristar 3020 Surface Area and Porosimetry analyzer. Prior to N_2 adsorption, the samples were degassed at 250 °C for 2 h. The N_2 adsorption-desorption isotherms were measured at −196 °C.

The X-ray diffraction patterns (XRD) were recorded using a Siemens D5000 diffractometer with the 0.02° step size and 1 s step time. The Cu Kα radiation (40 kV and 30 mA) was used as the X-ray source. The crystalline phases were identified by comparing the diffraction patterns with those of the standard powder XRD files (JCPDS) published by the International Center for Diffraction Data.

Quantitative elemental analyses were performed by inductively coupled plasma-optic emission spectroscopy 720-ES ICP-OES (Agilent) with axially viewing and simultaneous CCD detection. The quantitative determination of metal content in the catalysts was made based on the analysis of certificated standard solutions. The ICP ExpertTM software (version 2.0.4) provided metal concentration in the samples allowing estimating the weight percentage of components. The H_2 temperature-programmed reduction (H_2-TPR) experiments were carried out by the AutoChem II 2920 apparatus (Micromeritics) using 0.05 g of the sample in a flow of H2/Ar (5 vol. % H_2) stream (30 ml/min). The temperature was increased from room temperature to 900 °C at a rate of 10 °C/min.

The TEM (Transmission Electron Microscopy) analyses were carried out on a Jeol 2100 F (field emission gun) microscope operating at 200 kV equipped with a probe corrector for the spherical aberrations. The point-to-point resolution reached was on the order of 2 Å under the parallel TEM mode and 1 Å under the STEM (Scanning TEM) mode. For a better chemical resolution, the micrographs were also acquired in the HAADF mode by using a spot size of 1.1 Å with a current density of 0.5 pA $Å^{-1}$. More than 250 particles were counted to estimate the average Fe particle size and standard deviation from TEM images.

The in-situ XPS spectra were recorded using a VG ESCALAB 220 XL spectrometer using the Al Kα source (1486.6 eV). The powder samples were pressed into 6 mm diameter pellets. In each experiment, the XPS spectra of the fresh catalyst were first measured and then the pelleted catalyst was placed into the in-situ reaction cell heated under a flow of CO (50 mL/min, 1 bar) from room temperature to 350 °C at a heating rate of 10 °C/min and kept for 3 h. The treated sample was then transferred under vacuum without exposure to air to the analytical chamber to record the XPS spectra of the catalyst. After that, the catalyst was treated with H_2/CO mixture (50 mL/min, 1 bar) at 350 °C for 3 h in the reaction cell, and transferred under vacuum to the analytical chamber to record the XPS spectra of the reacted catalyst. The binding energies were corrected with respect to C 1 s of 284.6 eV and the binding energies were estimated within ± 0.2 eV.

The ^{57}Fe Mössbauer spectra were recorded in a transmission mode on a constant acceleration Mossbauer spectrometer (MS1104, Rostov-na-Donu, Rossia) with a ^{57}Co/Rh source, equipped with a liquid nitrogen cryostat. The fitting procedure was performed with custom software. All isomer shifts (IS) were referenced to ^{57}Fe in α-Fe at 300 K.

The magnetic properties of the catalysts were investigated *in situ* using a Föner vibrating-sample magnetometer [37,38] with the 10 mg catalyst loading. The magnetometer was calibrated using 1 mg of pure metallic Fe before each experiment. First, the sample was heated to 200 °C with a 6.6 °C/min ramping under 15 cm^3/min feed of pure CO and kept for 10 min and then sequentially heated to 350 °C with a 4.7 °C/min ramping and kept for 120 min. After the activation, the sample was cooled to the room temperature in the flow of CO. During the whole treatment, the saturation magnetization curve was recorded by the magnetometer. The pretreatment with syngas was performed using the same procedure.

2.3. Catalytic tests

The syngas conversion was performed in a fixed-bed reactor (8 mm inner diameter). Typically, the calcined catalyst (0.20 g, 100–150 μm) was loaded in the stainless-steel reactor and then activated in the CO gas flow (50 ml/min, atmospheric pressure) at 350 °C with a heating rate of 2 °C/min for 10 h before the reaction. The activation procedure was chosen on the basis of our previous publication [39]. After the reactor was cooled down to 180 °C, a syngas with a H_2/CO ratio of 1/1 and a pressure of 10 bar was introduced into the reactor. Nitrogen with a fixed flow rate of 1 ml/min in the syngas was used as an internal standard for the calculation of CO conversion. The temperature was raised with the ramping rate of 1 °C/min to the desired reaction temperature (350 °C). The catalytic test was conducted at 10 bar and 350 °C with syngas (H_2/CO = 1). GHSV has been varied in the range 3.4–20.4 L h^{-1} g^{-1}.

The reaction products were analyzed using a gas chromatograph (Bruker GC-450), which was equipped with a thermal conductivity (TCD) and a flame ionization (FID) detectors. Analysis of N2, CO, CO_2, and CH_4 was performed using a packed CTR-1 column and a TCD detector. The C1–C5 hydrocarbons were separated in a capillary Rt-Q PLOT column and analyzed by a FID detector. The liquid products (oil and water phases) were collected in a trap kept at 20 °C and analyzed off-line by gas chromatography. The selectivities were calculated on a molar carbon basis. Iron time yields (FTY) were expressed as moles of CO converted per gram of total iron per second. The product selectivities were reported as percentage of CO converted into a given product, respectively, and expressed on carbon basis. The CO_2 free hydrocarbon selectivities were calculated taking into account only hydrocarbon production in FT synthesis. The carbon balance was better than 90%. The chain growth probabilities, α, were calculated for the C_5-C_{12} hydrocarbon range from the slope of the curve $ln(S_n/n)$ versus n, where n is the carbon number of the hydrocarbon and S_n is the selectivity to the corresponding hydrocarbon.

For the Water-Gas Shift (WGS) reaction, 0.2 g of the as-prepared catalyst was placed in a stainless-steel tubular fixed bed reactor and then reduced at 400 °C for 1 h under hydrogen flow (50 ml/min). The temperature after the reduction was decreased to 180 °C. Prior to the reaction, the catalyst was first heated in N_2 atmosphere from 180 °C to 350 °C, then water steam was added to the mixture and then CO was introduced to the reactor. The products were analyzed using the same gas chromatograph as for FT reaction.

3. Results and discussion

3.1. Calcined catalysts

Table 1 shows textural properties and elemental composition of the CNT support and iron catalysts supported over CNT calcined in nitrogen. The pristine CNT has the BET surface area of 143 m^2/g and pore volume of 0.55 cm^3/g. The impregnation of CNT with iron and

Table 1
Physical properties of supports and supported Fe catalysts.

Sample	S_{BET}[a](m^2/g)	V_{tot}[b](cm^3/g)	D_{meso}[c](nm)	D_{Fe}[d](nm)	Total H_2 Consumption[e](mmol/g)	Reduct. degree[e](%)	Fe content[f](wt%)	Bi or Pb content[f](wt%)
CNT	143	0.55	15.4				–	–
Fe/CNT	131	0.45	13.9	6.3	1.28	33.3	11.4	–
FeBi/CNT	127	0.47	12.3	5.9	2.04	41.4	10.9	0.82
FePb/CNT	120	0.48	13.1	6.5	1.66	39.2	11.2	0.86

[a] BET surface area.
[b] Single point desorption total pore volume of pores, P/P_0 = 0.975.
[c] The pore diameter in the mesoporous region evaluated by the BJH method.
[d] Average particle size of iron oxide by TEM.
[e] The total H_2 consumption and iron reducibility degree from TPR analysis.
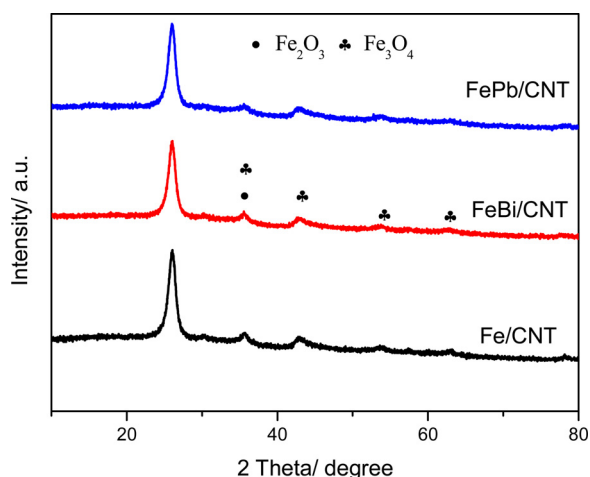[f] The Fe, Bi and Pb content from ICP-OES.

Fig. 1. XRD patterns of the Fe/CNT, FeBi/CNT and FePb/CNT catalysts calcined in nitrogen.

Fig. 3. H_2-TPR profiles of Fe/CNT, FeBi/CNT and FePb/CNT.

promoters decreases both the surface area and pore volume. The effect can be due to two phenomena. First, introduction of iron may result in the effect of "dilution" of carbon nanotubes with iron. Second, the impregnation can lead to blocking of CNT inner channels with iron species and promoters (Table 1).

The elemental analysis data are displayed in Table 1. All the catalysts showed similar iron content (around 10%) which is close to inventory, while the content of Bi and Pb were 0.82 wt. % and 0.86 wt. %, respectively.

Fig. 1 displays XRD profiles of the catalysts calcined in nitrogen. The peaks at 26.3° and 43.8° are attributed to the (002) and (101) reflections of the CNT supports. The diffraction lines at 2θ of 35.6° are
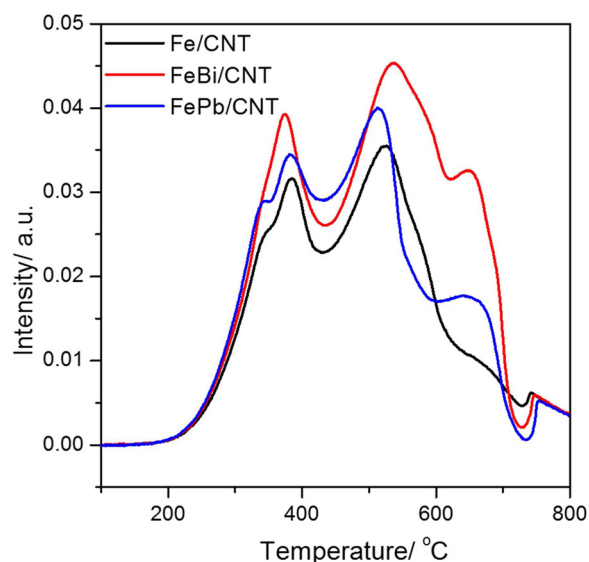
assignable to the hematite phase (Fe_2O_3, JCPDS 13-0534), while the diffraction lines at 2θ of 35.8°, 43.5° and 53.9° can be ascribed to the magnetite phase (Fe_3O_4, JCPDS 75-0449). The results are similar to previous reports, which showed that decomposition of iron nitrate in nitrogen results in the formation of mostly the magnetite phase [19,40]. The XRD profiles also suggest that adding Bi or Pb does not modify the iron oxide phase composition in the calcined catalysts.

Fig. 2 displays TEM images of the calcined unpromoted and promoted iron catalysts. Carbon nanotubes and iron oxide nanoparticles are clearly observed. Quantitative analysis using particle size
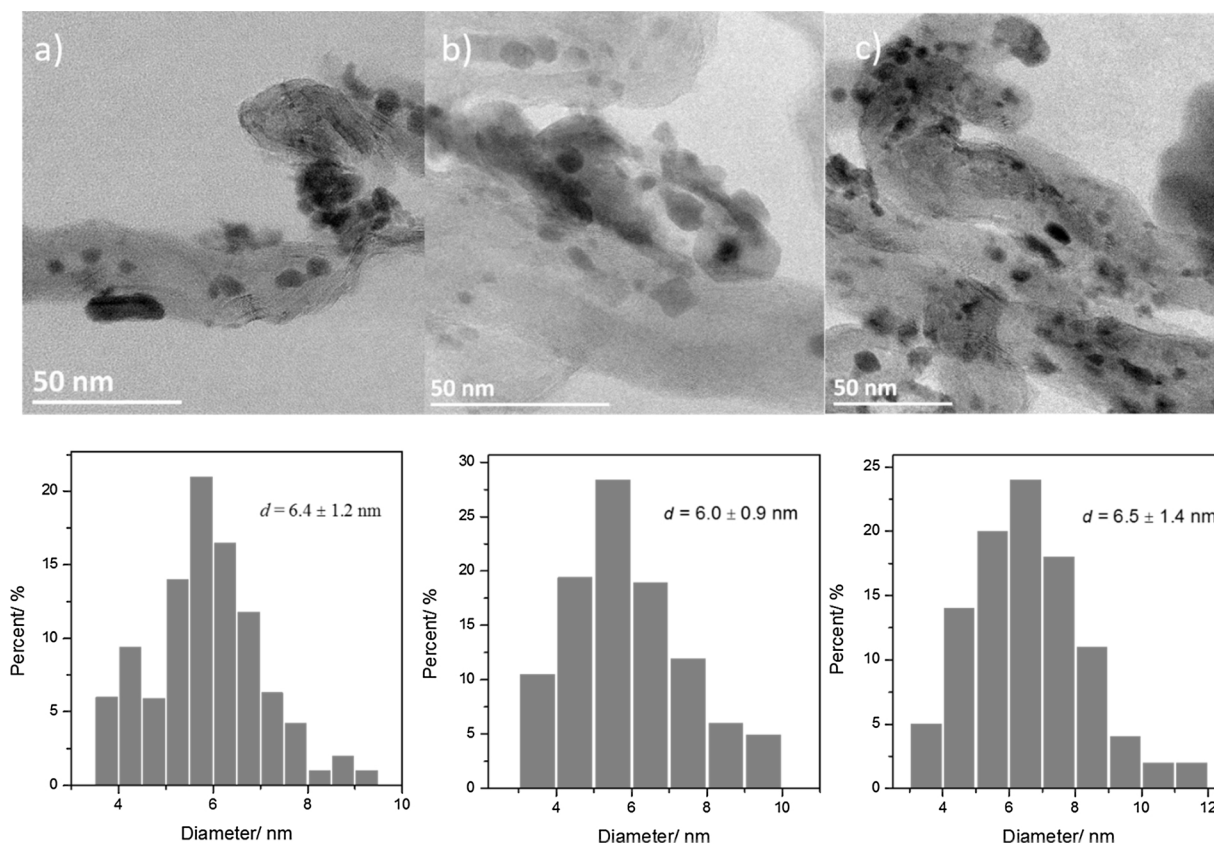

Fig. 2. TEM micrographs and particle size distributions for fresh Fe catalysts: (a) Fe/CNT, (b) FeBi/CNT and (c) FePb/CNT.
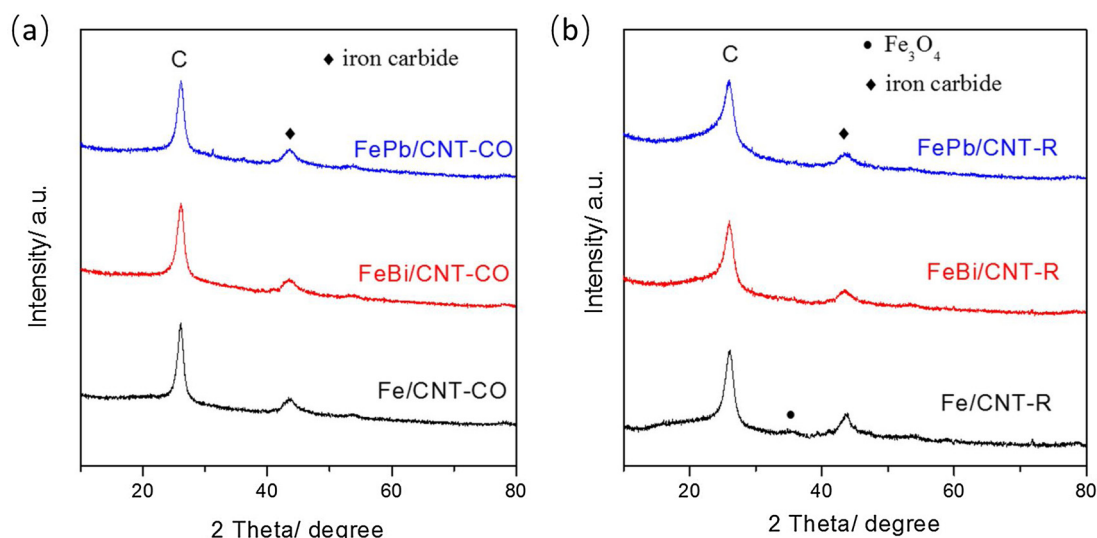
Fig. 4. XRD profiles the catalysts: (a) after treatment at 350 °C for 10 h under CO gas flow, (b) the used catalysts.
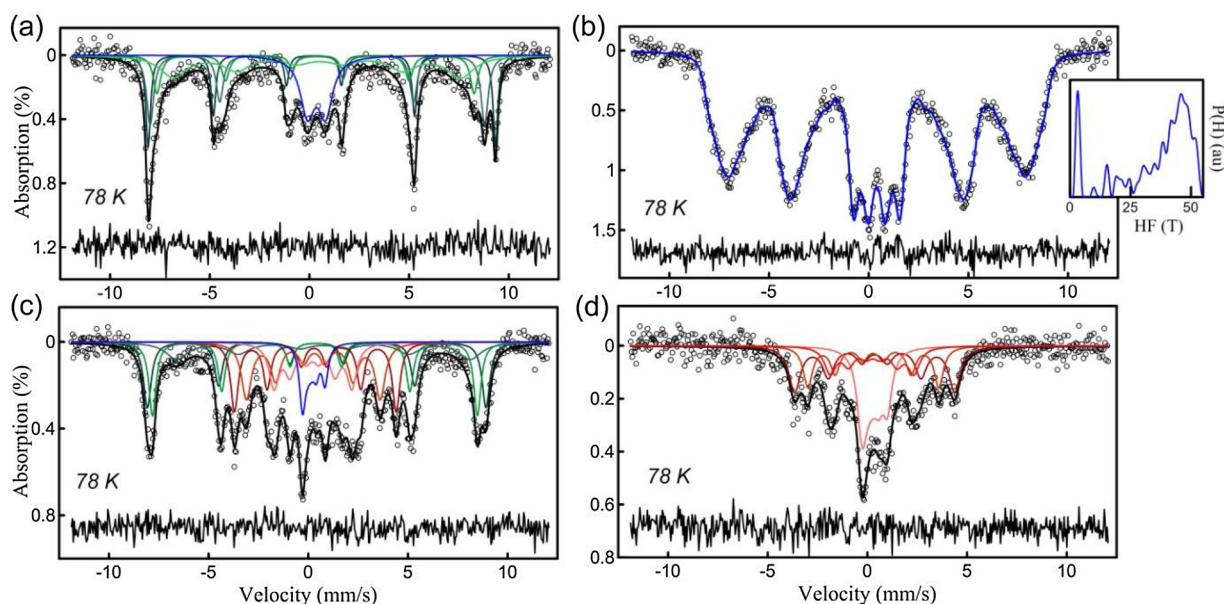

Fig. 5. Mössbauer spectra of the fresh and used catalysts, measured at 78K: (a) Fe/CNT, (b) FePb/CNT, (c) Fe/CNT-used, (d) FePb/CNT-used.

histograms also give the average iron oxide nanoparticle diameters of 5–6 nm, which is consistent with the XRD data. Interestingly, the sizes of iron oxide crystallites are not affected by the promotion. This suggests that the promotion of iron catalysts with Bi and Pb does not affect to any noticeable extent iron dispersion.

Reducibility is another essential parameter of iron catalysts. Fig. 3 shows the H_2-TPR profiles of the un-promoted Fe/CNT catalyst and Bi- and Pb-promoted counterparts. Three main groups of hydrogen consumption peaks were observed for all the catalysts. The reduction of iron oxides is a stepwise process, which occurs as follows: $Fe_2O_3 \rightarrow Fe_3O_4 \rightarrow FeO \rightarrow Fe$ [41,42,43]. The TPR peaks were, however, very broad. This can be due to broad iron particle size distribution, metal-support interactions, promotion effects or temperature ramping rate. Generally, the first TPR peak at 250–420 °C can be assigned to the reduction of Fe_2O_3 to Fe_3O_4, the second peak can be ascribed to the reduction of Fe_3O_4 to FeO and the third peak (600–700 °C) can be attributed to the reduction of FeO to Fe°. The broad peak above 720 °C can be caused by gasification of the CNT support [35,40]. Note that the molar concentrations of Bi and Pb were 50 times lower than iron. Even

if the Bi and Pb promoters can be reduced under these conditions, no visible TPR peaks are expected during the reduction of promoters. Fig. 3 also shows that the presence of Bi and Pb promoters shifts the reduction peaks from 250 to 420 °C to lower temperature. Similar results were obtained with iron catalysts supported on carbon nanotubes promoted with Mn [35]. Interestingly, higher intensity of the TPR peaks, which are assigned to the FeO reduction to metallic Fe was observed on the Bi and Pb promoted catalysts. This suggests that the presence of these elements facilitates formation of iron metallic phases. The total hydrogen consumption during TPR experiments is an important parameter, which provides information about the reducibility of supported iron species. TPR results therefore suggest the following sequence of studied iron catalysts relative to total hydrogen consumption and iron reducibility: Fe/CNT < FeBi/CNT < FePb/CNT (Table 1).

3.2. Carbidized iron catalysts

Iron carbides, which are generated in the presence of carbon monoxide or syngas are usually considered as active phase for FT synthesis.

Table 2
78K Mössbauer data of the fresh and used catalysts.

Sample	Mössbauer parameters[a]				Phase	Area (%)
	δ(mm/ s)	ΔEQ (mm/ s)	H (T)	Γ (mm/ s)		
Fe/CNT	0.49	0.39	54.1	0.28	Fe^{3+}, Fe_2O_3 well crystalline	20
	0.45	0.04	52.1	0.43	Fe^{3+}, presumable γ-Fe_2O_3	23
	0.42	−0.09	49.4	0.44	Fe^{3+}, Fe_2O_3 poor crystalline (I)	13
	0.51	−0.14	44.7	1.62	Fe^{3+}, Fe_2O_3 poor crystalline (II)	27
	0.42	0.91	–	0.86	Fe^{3+}, superparamagnetic	18
Fe/CNT-used	0.49	0.00	52.7	0.47	Fe^{3+}, Fe_2O_3	16
	0.83	0.00	45.7	1.34	Fe^{3+}, Fe_3O_4 and/or γ-Fe_2O_3	12
	0.42	−0.05	50.6	0.43	Fe^{2+}, Fe_3O_4	16
	0.39	0.07	25.2	0.46	Fe^{3+}, Fe_5C_2 (I)	16
	0.35	−0.05	20.8	0.60	Fe^{3+}, Fe_5C_2 (II)	17
	0.29	0.02	12.1	0.60	Fe^{3+}, Fe_5C_2 (III)	12
	0.24	0.20	3.6	0.36	Fe carbide and/or oxide Fe^{3+}, superparamagnetic	11
FePb/CNT	0.48	0	< 5-55 >	–	Fe^{3+}, superparamagnetic Fe_2O_3	100
FePb/C T-used	0.43	0.00	24.9	0.70	χ-Fe_5C_2 (I)	32
	0.36	0.01	20.4	0.56	χ-Fe_5C_2 (II)	23
	0.32	−0.04	13.0	0.70	χ-Fe_5C_2 (III)	19
	0.34	0.15	4.1	0.55	Fe_{carb} and/or oxide Fe^{3+}, superparamagnetic	26

[a] δ (mm/s) = isomer shift (± 0.01 mm/s), ΔEQ (mm/s) = quadrupole splitting (± 002 mm/s). H (T) = hyperfine magnetic field (± 002 T), Γ (mm/s) = linewidth (± 0.02 mm/s). Isomer shifts are relative to α-Fe.
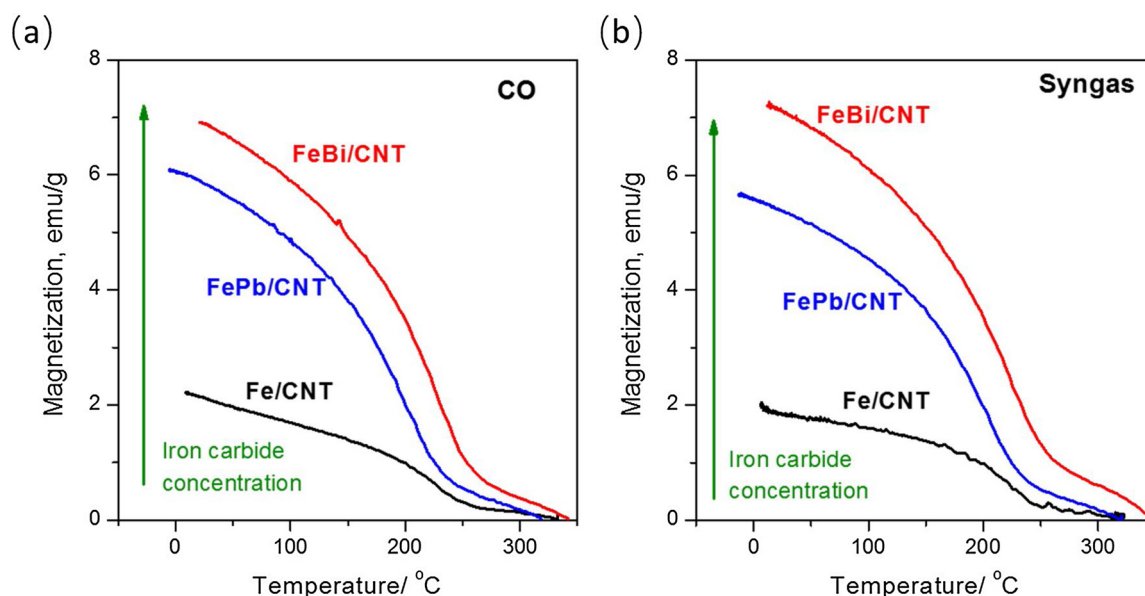
Fig. 6. Catalyst magnetization measured: (a) during cooling down after CO treatment at 350 °C, (b) during cooling down after syngas treatment at 350 °C.

The catalysts were exposed to the flow of CO at 350 °C for iron carbidisation. Fig. 4a shows the XRD profiles of the catalysts after the treatment under CO at 350 °C for 10 h. A broad diffraction peak is observed at ca. 44° irrespective of the catalyst composition. This broad peak can be assigned to iron carbides, indicating that iron oxides are converted into iron carbides during the CO pretreatment.

Several iron carbides such as Fe_3C, χ-Fe_5C_2, ε-$Fe_{2.2}C$ can be present in the carbidized iron catalysts. The identification of individual iron carbide phases can be only performed for larger iron carbide crystals, which exhibit relatively distinct and well resolved XRD peaks. A comparison of the XRD peaks of the activated catalysts with those observed for the iron carbide reference compounds indicates the presence of either χ-Fe_5C_2 or ε-Fe_2C in the activated catalysts. Note that XRD characterization nearly excludes the presence of θ-Fe_3C or Fe_7C_3. Due to a significant broadening and overlapping of the carbide XRD peaks, the unambiguous identification of specific χ-Fe_5C_2 or ε-Fe_2C carbide phases seems rather challenging from XRD patterns. A weak peak at ca. 52.5° of magnetite is also detected which may be caused either by incomplete

carbidisation of iron oxides or by the surface oxidation during the sample transfer and XRD acquisition.

The iron phases in the fresh and used catalysts were analyzed by the Mössbauer spectrometry (Fig. 5). The fresh catalysts mainly contain Fe_2O_3 phase, the used FePb/CNT catalyst generates much more χ-Fe_5C_2 than the used Fe/CNT catalyst with relative areas of 74% and 45%, respectively (Table 2). Note that superparamagnetic components in the spectra are most probably belong to carbides (smallest particles). So, the carbide contributions for the used FePb/CNT catalyst could be even higher.

The in situ magnetic measurements were performed at different temperatures under the flow of carbon monoxide and syngas. They have provided more specific and quantitative information about type and concentration of iron carbides in supported iron catalysts. Prior to the in-situ magnetic measurements, the catalysts were carbidized in a flow of carbon monoxide at 350 °C. Fig. 6 shows variation of catalyst magnetization with temperature during cooling of the samples after the carbidisation in CO or syngas. The shapes of thermomagnetic curves
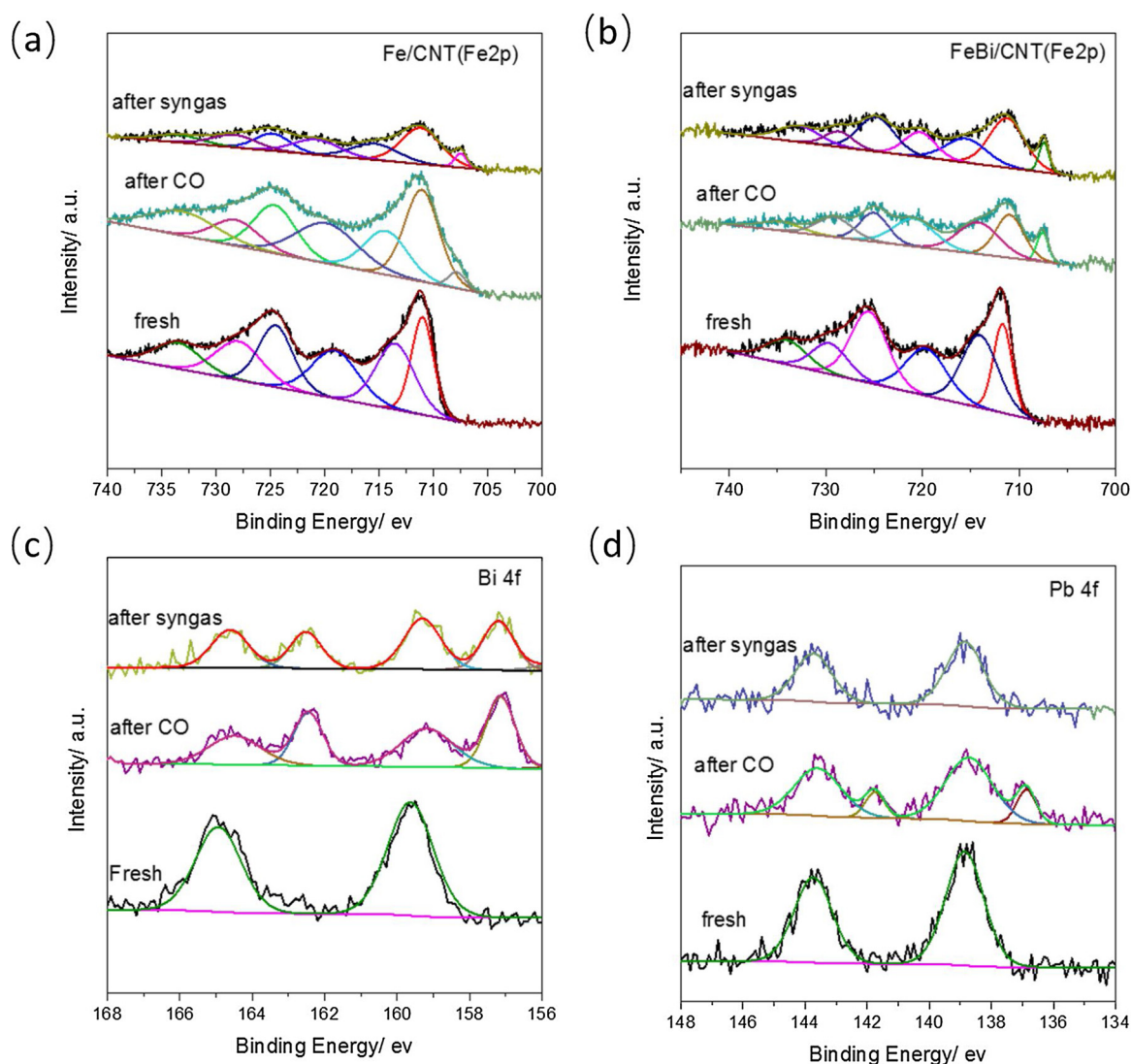
Fig. 7. a) Fe 2p XPS spectra of the Fe/CNT catalyst after calcination, exposure to carbon monoxide and syngas, b) Fe 2p XPS spectra of the FeBi/CNT catalyst after calcination, exposure to carbon monoxide and syngas, c) Bi 4f XPS spectra of the FeBi/CNT catalyst after calcination, exposure to carbon monoxide and syngas, d) Pb 4f XPS spectra of the FePb/CNT catalyst after calcination, exposure to carbon monoxide and syngas.

Table 3
Catalytic performances of supported Fe catalysts for FT synthesis.[a]

| Catalyst	Reaction condition		FTY,10^{-4} mol$_{Fe}^{-1}$s^{-1}	CO conv. (%)	CO$_2$ select. (%)	Hydrocarbon selectivity (%)				C$_{2-4}^=$/ C$_{2-4}^\circ$	α values
	P Bar	GHSV Lg^{-1}h^{-1}				CH$_4$	C$_{2-4}^=$	C$_{2-4}^\circ$	C$_{5+}$		
Fe/SiO$_2$	10	3.4	0.2	10.1	29	26.4	29.6	25.4	18.8	1.17	0.47
Fe/CNT	10	3.4	1.0	57.3	40	29.1	32.4	17.3	21.9	1.87	0.55
	1	3.4	0.09	4.5	23	31.0	49	7.4	12.6	6.6	0.48
FeBi/CNT	10	3.4	1.6	78.3	47	26.1	35.2	25.6	14.1	1.38	0.43
	10	13.6	4.2	50.7	46	26.5	36.1	15.6	21.8	2.31	0.42
	1	3.4	0.2	10.0	33	28.1	60.9	6.1	3.9	10.0	0.34
FePb/CNT	10	3.4	2.0	96	50	22.4	28.4	20.8	28.4	1.37	0.50
	10	13.6	4.8	56.8	48	27.7	35.8	18.7	17.7	1.91	0.47
	1	3.4	0.4	18.6	35	25.6	57.7	7.4	9.3	7.80	0.36
Fe/CNT + Bi/CNT	10	3.4	1.4	67.6	43	26.5	34.5	26.9	12.1	1.28	0.46
Fe/CNT + Pb/CNT	10	3.4	1.6	77.6	44	23.6	32.6	18.3	25.5	1.78	0.48
Bi/CNT or Pb/CNT	10	3.4	0	0	0	0	0	0	0	0	–

[a] Reaction conditions: W = 0.2 g, H$_2$/CO = 1, T = 350 °C, P = 10 bar or 1 bar, time on stream = 20 h.

obtained after carbidisation in CO and syngas are very similar. Low magnetization at higher temperatures could be due to the disordering of magnetic domains after attaining the Curie temperature for the ferromagnetic phases present in the activated catalysts. Several iron ferromagnetic compounds may exist: iron carbides, metallic iron and magnetite (Fe$_3$O$_4$). The Curie temperature for these compounds is given in our previous report [19]. Indeed, the Curie temperature of χ-Fe$_5$C$_2$ is close to 250 °C, while the Curie temperatures of magnetite and metallic
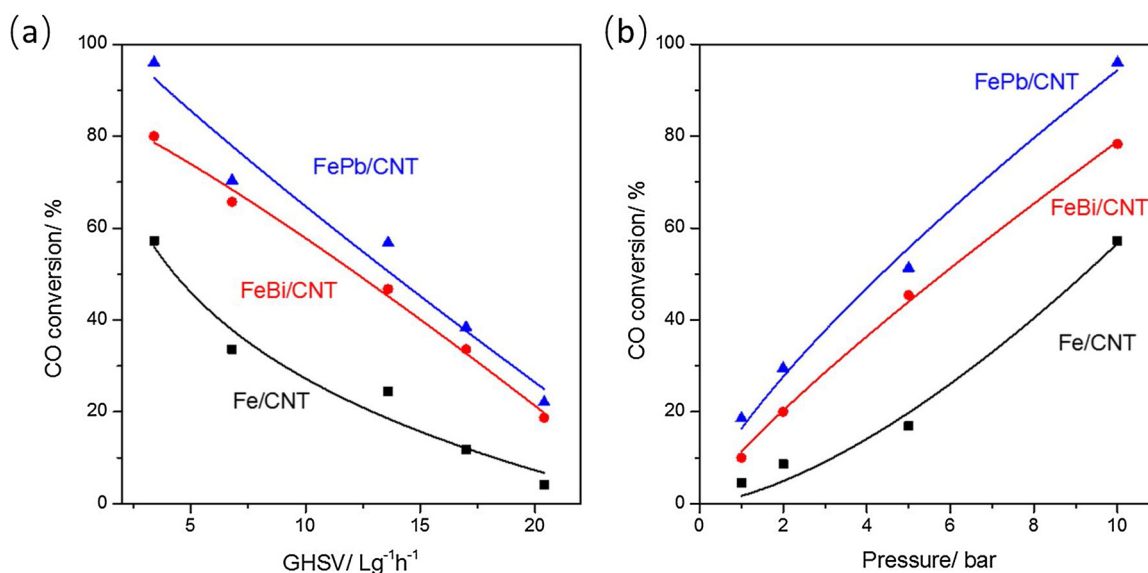
Fig. 8. Carbon monoxide conversion over CNT supported iron catalysts under different reaction condition: (a) under different GHSV, P = 10 bar, (b) under different pressure, GHSV = 3.4 L h^{-1} g^{-1}. Reaction conditions: W = 0.2 g, H$_2$/CO = 1, P = 1–10 bar, T = 350 °C, GHSV = 3.4–20.4 L h^{-1} g^{-1}.
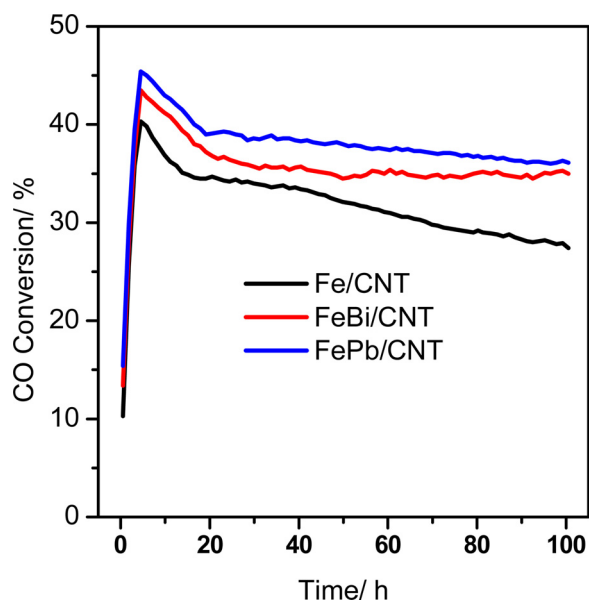
Fig. 9. Carbon monoxide conversion as a function of tie of stream for the pristine Fe/CNT and Bi and Pb promoted catalysts (H$_2$/CO = 1, P = 10 bar, T = 350 °C, GHSV for Fe/CNT 6.8 L g^{-1}h^{-1}, FeBi/CNT and FePb/CNT 17 L g^{-1}h^{-1}).

iron are 580 and 770 °C, respectively [19,44]. Note that a decrease in magnetization to zero at temperatures higher than 300 °C rules out the presence of any noticeable concentrations of metallic iron, magnetite or hexagonal ε-Fe$_2$C carbide (T$_{Curie}$ = 380 °C). All these compounds have relatively high Curie temperature. The presence of θ-Fe$_3$C in the activated catalysts has been already excluded by the XRD data.

The Curie temperature was evaluated from the first derivative of the magnetization variation with temperature. The unpromoted Fe/CNT and Bi- and Pb promoted catalysts exhibit the presence of Hägg χ-Fe$_5$C$_2$ iron carbide, which has the Curie temperature around 250 °C. Besides of χ-Fe$_5$C$_2$, a small concentration of ferromagnetic phase with the Curie temperature at 280 °C was detected. This phase cannot be attributed to any known iron bulk phase. Indeed, all known iron phases do not have Curie temperature in this range [19]. This phase was tentatively attributed to non-stoichiometric iron carbide species.

It is important to emphasize that in the CNT supported catalysts activated in CO and exposed to syngas, the thermomagnetic curves shown in Fig. 5 are indicative of iron carbides as the only ferromagnetic phases. Thus, the saturation magnetization can be directly related to the iron carbide concentration. Therefore, the extent of carbidisation can be estimated from the total magnetization at a given temperature. The magnetization results are indicative of higher magnetization of the Bi- and Pb- promoted catalysts compared to the unpromoted Fe/CNT. These catalysts have the same iron content. Higher magnetization observed in the promoted catalysts is therefore indicative of higher extent of iron carbidisation. After activation in CO, higher amount of the Hägg iron carbide was observed in the promoted catalysts compared to the unpromoted one. This observation correlates with Mössbauer data, which were also indicative of higher extent of iron carbidisation in the promoted catalysts.

The subsurface structure of iron catalysts was investigated by XPS (Fig. 7). The catalyst was transferred from the pre-treatment chamber to the XPS analysis chamber of the spectrometer without exposure to air. The Fe 2p XPS spectra (Fig. 7a and b) display peaks at 710.9 and 724.1 eV in a 2:1 peak area ratio, which are assigned to the Fe 2p$_{3/2}$ and Fe 2p$_{1/2}$ signals, respectively. The spectra are typical for the Fe^{3+} species in Fe$_2$O$_3$ [45] (Fig. 7a). After treatment with CO at 350 °C for 120 min, the XPS peaks attributed to Fe^{3+} significantly decrease in intensity. A broad peak with the binding energy of 707.3 eV assignable to iron carbide (Fe$_5$C$_2$) was detected [45,46]. This suggests coexistence of the iron oxide and iron carbide in the activated catalysts. When the activated Fe/CNT sample was exposed to a mixture of CO/H$_2$ = 1 (v/v) at 350 °C for 120 min, the intensity of XPS peak at 707.3 eV increases. A higher amount of iron carbide seems to have been formed during the catalyst exposure in syngas. Interestingly, the intensity of iron carbide XPS peaks at 707 eV was much higher in the Bi-promoted catalyst. This is also consistent with higher extent of iron carbidisation in the promoted catalysts compared to the unpromoted counterpart.

The Bi 4f XPS data were indicative of the presence of Bi in the oxidized state after calcination (Fig. 7c). The peaks with binding energies of 158.6 and 165 eV [47] were observed. Catalyst activation in carbon monoxide leads to partial Bi reduction to metallic state with a characteristic XPS peak at 156.9 eV [48]. This suggests that catalyst treatment with carbon monoxide results in the removal of oxygen atoms from the promoter. Importantly, bismuth also remains in the metallic state after the subsequent exposure to syngas.

Slightly different phenomena were observed by XPS for the lead
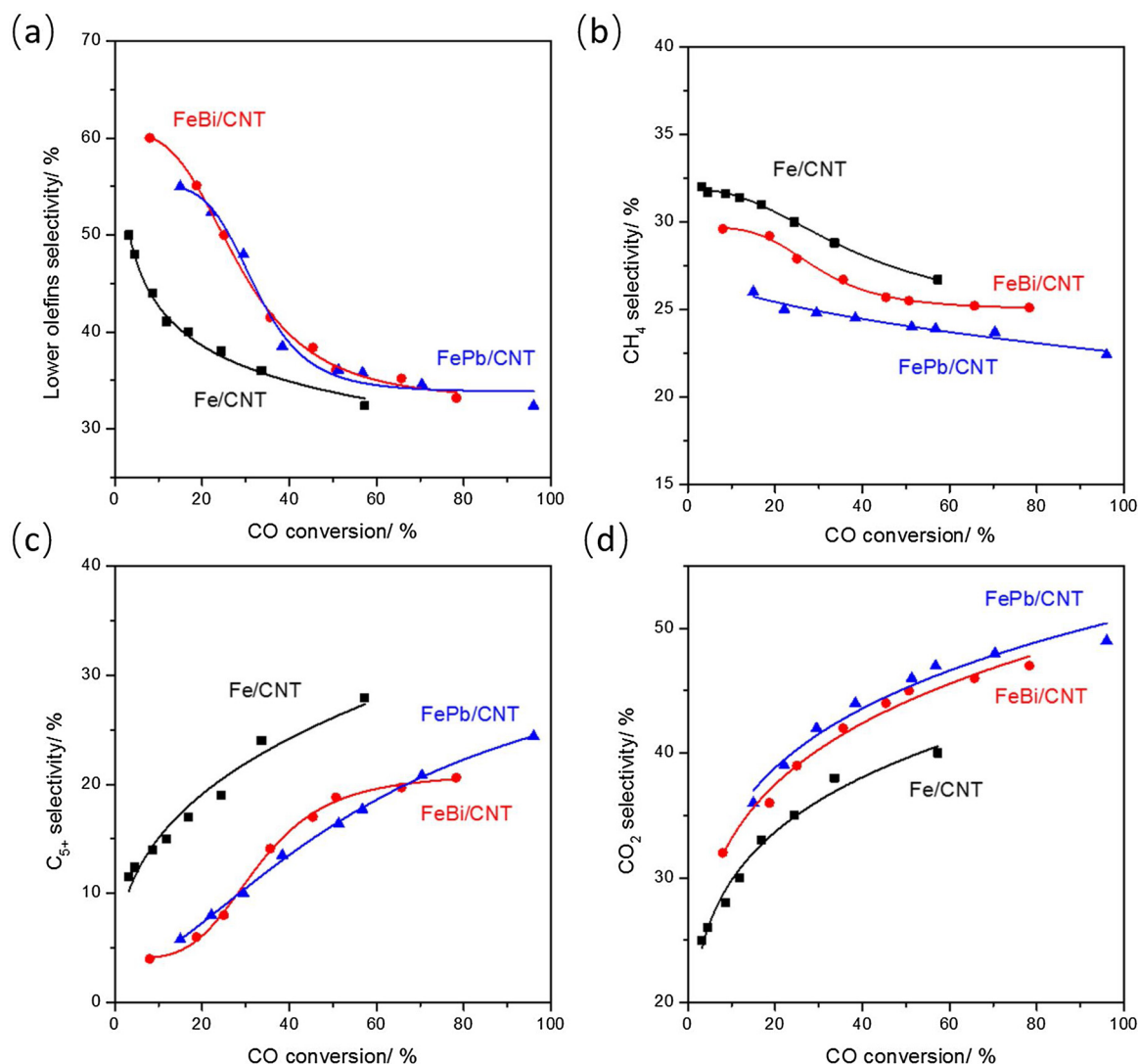
Fig. 10. Product selectivity versus CO conversion over CNT supported iron catalysts. Reaction conditions: W = 0.2 g, H_2/CO = 1, P = 10 bar, T = 350 °C, $GHSV$ = 3.4–20.4 L h^{-1} g^{-1}.

promoted catalysts. The Pb 4f XPS spectra were indicative of the presence of Pb in the oxidized state after calcination (Fig. 7d). Similar to the Bi-promoted catalyst, activation in CO results in partial Pb reduction. Note however that different to FeBi/CNT, exposure of FePb/CNT to syngas results in lead oxidation. Lead can easily change oxidation state during FT reaction. After syngas treatment, Bi is present in both metallic and oxide states, however the Pb remains oxide state. The oxidation state of lead seems much more sensitive to the reaction environment [28]. This is also consistent with the electrochemical potentials of bismuth and lead (+ 0.317 V and –0.126 V respectively). Variation of the oxidation states of the Bi and Pb promoters is essential for the enhanced catalytic performance. The promoters, which are located at the interface of iron carbide particles, facilitate CO dissociation by scavenging O atoms. The reasons of lead and bismuth oxidation during FT reaction are discussed in Section 3.4.

3.3. Catalytic results

The catalytic data for the CNT supported Fe catalysts promoted with Bi and Pb are shown in Table 3. Table 3 also displays the catalytic data obtained under the same conditions for the Fe/SiO$_2$ catalyst. The data for Fe/SiO$_2$ are given for comparison. Methane, C$_2$-C$_4$ light olefins, C$_{5+}$ hydrocarbons, carbon dioxide and water were the products of syngas

conversion over the iron catalysts. Iron supported on CNT showed around 5 times higher CO conversion compared with the SiO$_2$ supported iron catalyst under the same conditions. These results are consistent with previous reports about the catalytic performance of iron catalysts in FT synthesis. Indeed, iron catalysts supported on carbon materials have been shown to be usually more active than those loaded on SiO$_2$, because of higher carbidisation of iron [12,19] and possible electron dative effect from carbon [49] on iron species, which facilitates dissociation of carbon monoxide.

Importantly, promotion with Bi and Pb also produces a very strong effect on the catalytic activity of iron catalysts supported on carbon nanotubes. At GHSV = 3.4 nL/g$_{cat}$ h, the CO conversion increased from 57.3% observed over the Fe/CNT catalyst to 78.3% and 96% over the Bi and Pb-promoted counterparts, respectively (Table 3).

Fig. 8 shows the effects of pressure and GHSV on the CO conversion. At the same pressure, the CO conversion increases as the GHSV is decreasing. The result is rather expected and is due to the variation of the residence time. At iso-GHSV, the FT reaction rates on unpromoted and promoted catalysts increase with the pressure increase. Interestingly, the Bi or Pb promoted catalysts show higher CO conversion under both the same pressure and GHSV compared with the unpromoted iron catalyst. Interestingly, the promotion effect remains very significant even at low pressure (1 bar). While the carbon monoxide conversion
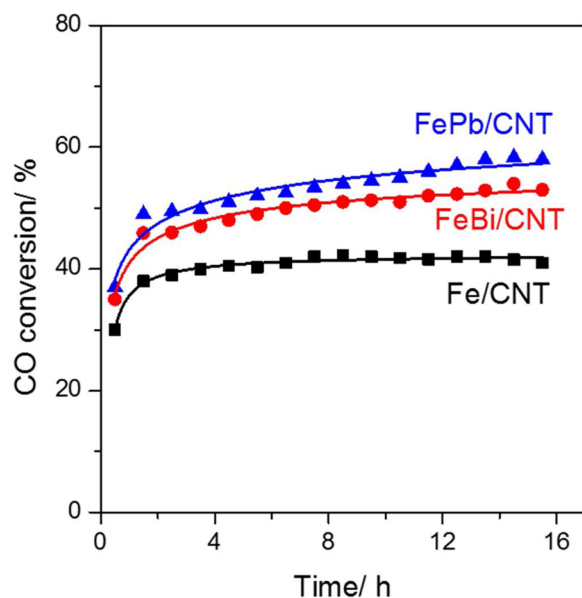
Fig. 11. CO conversion in Water-Gas Shift reaction over un-promoted and promoted iron catalysts. Reaction conditions: p = 1 bar, CO = 5 ml/min, N_2 = 30 ml/min, H_2O = 0.5 ml/h.

over the unpromoted Fe/CNT was very low (4.5%) at GHSV = 3.4 nL/gcat h at atmospheric pressure, the catalysts promoted with Bi and Pb showed noticeable CO conversions of 10–20% under the same conditions.

Promotion with Pb and Bi produces also a noticeable effect on the catalyst stability. Fig. 9 shows carbon monoxide conversion as a function of time on stream. Similar CO conversion were obtained by variation of GHSV. The promoted catalysts exhibit better stability compared to the pristine Fe/CNT.

Interestingly, over promoted catalysts the decrease in the pressure to 1 bar leads to increase in the selectivity to the C_2-C_4 olefins by about

20% reaching ~60% at the conversion levels of 10–20 % under the same conditions. The olefin yield from syngas observed under these conditions is one of the best reported so far in the literature [1] (Table 3). At the same time, lower reaction pressure also leads to lower C_{5+} hydrocarbon selectivity (Fig. 10). Note that the Bi- and Pb-promoted catalysts show much lower selectivity to light paraffins and C_{5+} hydrocarbons in comparison with the reference Fe/CNT unpromoted catalyst (Fig. 10, Table 3).

The observed selectivity phenomena also coincide with the gradual decrease in the chain growth probability (α) with the pressure decrease. The Anderson-Schulz-Flory distribution predicts maximum selectivity to the C_2-C_4 hydrocarbons of about 57% at α value of 0.46. The pressure decreases from 10 to 1 bar leads to lower α, which is favorable for the selectivity to light hydrocarbons. Indeed, it has been shown [50,51,52,53,54] that higher total pressure and low H_2/CO ratio is favorable for synthesis of long chain paraffinic hydrocarbon at the expense of light olefins. On the other hand, the Bi- and Pb- promoters seem to slow down secondary olefin hydrogenation and impose some restrictions on the FT chain growth probability. Indeed, the olefin to paraffin ratio in the products is much higher over the Bi- and Pb-promoted catalysts compared to the Fe/CNT and in particular at lower reaction pressure. Thus, use of the Bi- and Pb- promoters makes it possible to produce light olefins over iron catalysts with higher yield and selectivity under mild reaction conditions and in particular, at lower reaction pressures.

The product selectivities for the Bi and Pb promoted iron catalyst and Fe/CNT measured as a function of carbon monoxide conversion are summarized in Fig. 10 The selectivity to light olefins typically decreases with increasing CO conversion for the three examined catalysts (Table 3, Fig. 10). More importantly, the promoted iron catalysts showed higher selectivity to lower olefins in the similar CO conversion compared with the Fe/CNT catalysts. The presence of promoters stabilizes selectivity to light olefins at 10 bat at high conversion. The selectivity is close to 35% with suppression of the secondary transformation of olefins. This effect of the Bi and Pb promoters on the FT reaction selectivity is somewhat similar but more complex compared to
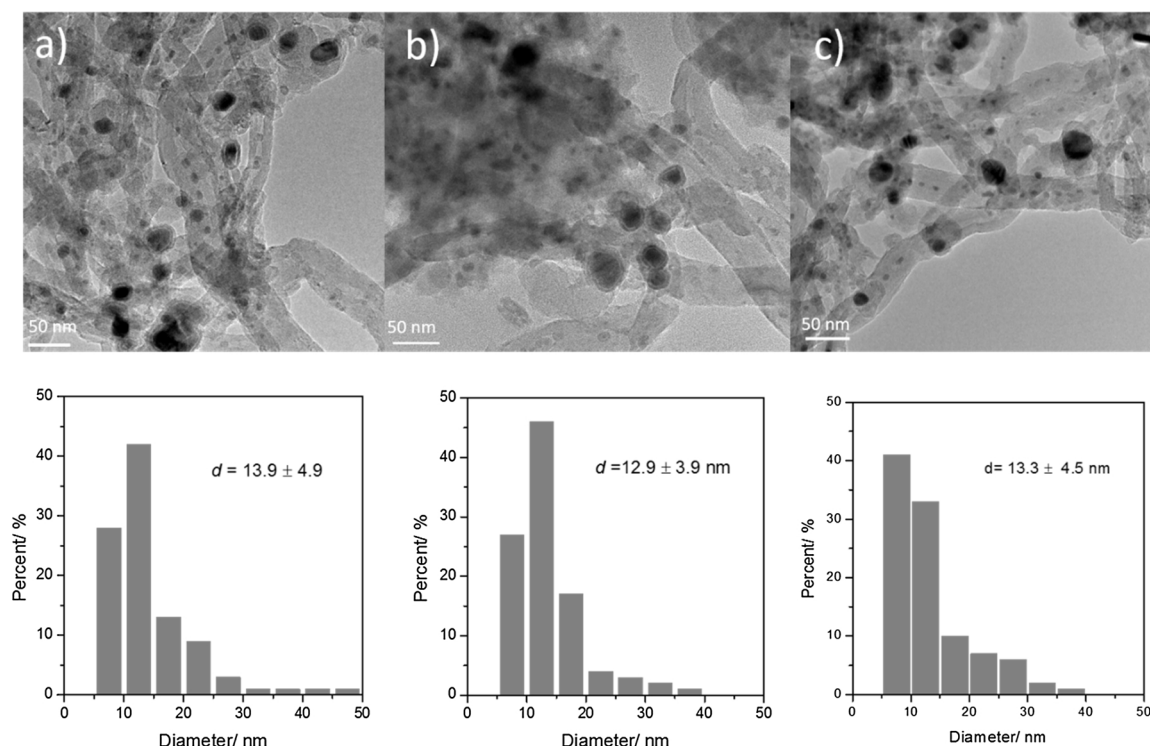
Fig. 12. TEM micrographs and particle size distributions for spent supported Fe catalysts after reaction: (a) Fe/CNT, (b) FeBi/CNT, (c) FePb/CNT.
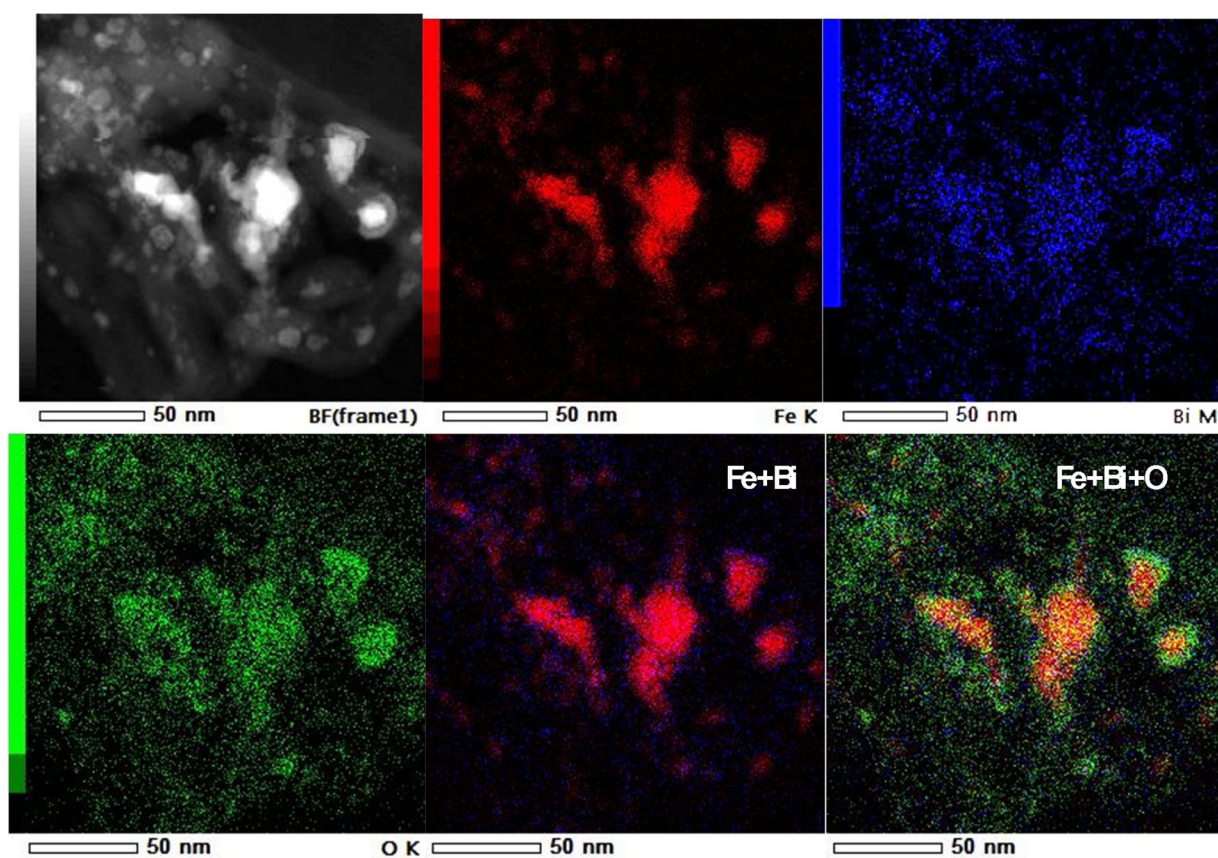
Fig. 13. STEM-HAADF image and EDX mapping of the activated FeBi/CNT catalyst (CO treatment for 10 h at 350 °C).
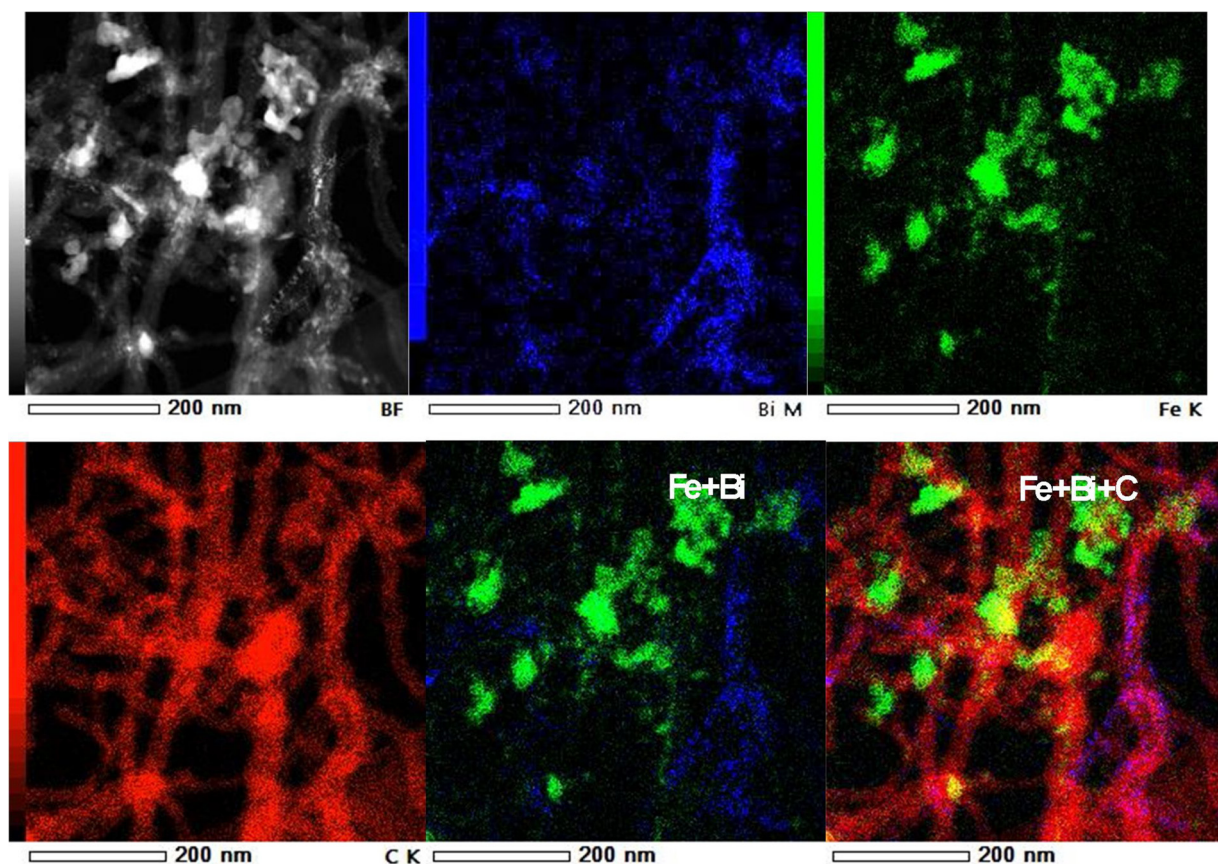

Fig. 14. STEM-HAADF image and EDX mapping of the mixed Fe/CNT + Bi/CNT catalyst calcined in nitrogen.
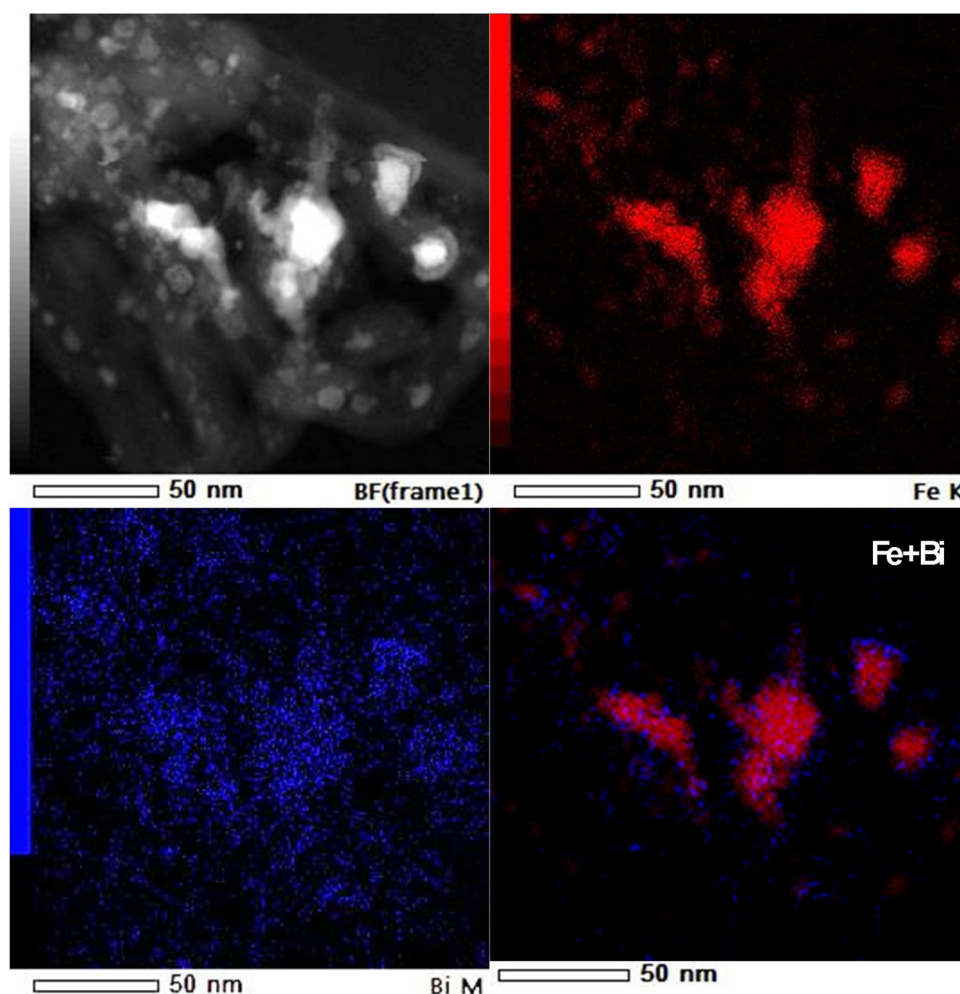
Fig. 15. STEM-HAADF image and EDX mapping of the activated mixed Fe/CNT + Bi/CNT catalyst after carbidisation in CO.

that observed in the presence of alkali promoters [16,20]. Indeed, the presence of alkali ions in iron catalysts leads to higher olefin to paraffin ratio in the FT reaction products. Note that the increase in the olefin to paraffin ratio over the catalysts promoted with alkali ions usually coincides with lower methane selectivity, higher selectivity to the long-chain hydrocarbons and an increase in the chain growth probability. Indeed, the Bi or Pb promoted catalysts exhibit lower selectivity to methane compared with Fe/CNT catalyst, this effect is also found in Na-[2,26] and Mn- [23] promoted iron catalysts for lower olefin synthesis. Different to the alkali promotion, however, the Bi and Pb-promoted catalysts exhibit lower selectivity to long chain hydrocarbons.

WGS is an important side reaction, which occurs during FT synthesis on iron catalysts. It yields water and CO_2, affects the H_2/CO ratio in the reactor and selectivity to different reaction products. Fig. 10d shows the CO_2 selectivity at different CO conversions. The selectivity of CO_2 over the promoted catalysts is higher than over the unprompted catalysts, which may be caused by the higher rate of WGS reaction. Carbon dioxide selectivity is also getting higher at higher carbon monoxide conversion. Water gas shift reaction $(CO + H_2O = CO_2 + H_2)$ represents one of the possible reaction pathways for the CO_2 production in FT synthesis. Usually, the WGS reaction is expected to be more significant at higher CO conversion when water production is getting more important. Note however, that over the Bi and Pb-promoted iron catalysts, high carbon dioxide selectivity is observed even at very low CO conversion levels. This suggests that over promoted catalysts, carbon dioxide can be among the primary reaction products and is produced during the initial reaction steps [28].

The performance of iron catalysts in the WGS reaction was also evaluated in a fixed bed reactor. The effect of Bi and Pb promoters on CO conversion for WGS reaction with time-on-stream is shown in Fig. 11. In the first 10 min, the CO conversion of Fe/CNT is 30%, while the Bi and Pb promoted catalysts show higher CO conversion, which are 35% and 37%, respectively. After 15 h time on stream, the CO conversion for Fe/CNT, FeBi/CNT and FePb/CNT are 40%, 52% and 59%, respectively (Fig. 11). This suggests that Bi and Pb improve the activity of iron catalysts in the WGS reaction. This effect was also found in alkali promoted iron catalysts [55].

3.4. Interaction of iron species with promoters and catalytic performance in FT synthesis

FT synthesis is a structure-sensitive reaction over metal and carbide catalysts. The catalytic activity and selectivity strongly depend on the catalyst structure and in particular on the metal or carbide particle size, especially in the nano-size range. For iron catalysts, previous reports [56] suggest the influence of particle size on the catalytic performance when the particle size is below 6 nm and negligible when the particle size is above 6 nm. XRD (Fig. 1) and TEM (Fig. 2) show that the particle sizes for the Fe/CNT and Bi or Pb promoted Fe/CNT catalysts were almost identical and in the range of 5.9–6.5 nm.

Fig. 12 displays the TEM images and histograms of iron nanoparticles in the catalysts after the FT reaction tests. The catalytic reaction results in some sintering of iron nanoparticles. Remarkably, while the size of iron carbide nanoparticle increases from 5 to 6 to
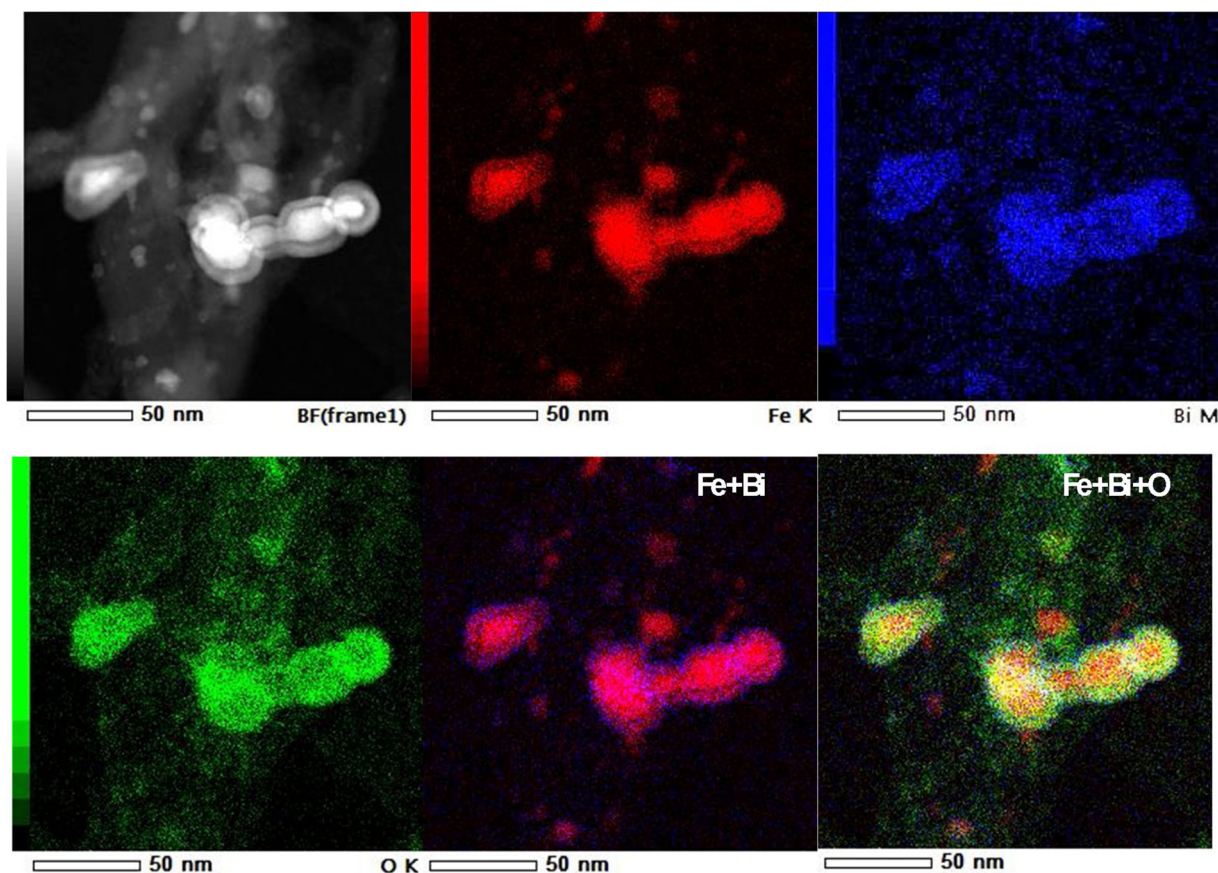
Fig. 16. STEM-HAADF image and EDX mapping of the spent mixed Fe/CNT + Bi/CNT catalyst (after the catalytic test).

12–14 nm during the reaction, the increase is the same for the un-promoted and promoted iron catalysts. This suggests that the promoters do not affect to any significant extent the rate of iron sintering in these catalysts. Thus, variation of iron particle size with promotion is not the crucial factor for their much different catalytic performances.

The second important parameter can be iron reducibility/carbidi-sation. Indeed, the TPR profile (Fig. 2) indicate some enhancement in iron reducibility especially for FeO→Fe reduction step in the promoted catalysts. The in-situ magnetization measurements also suggest better iron carbidisation in the promoted catalysts compared to the un-promoted counterpart. The magnetization data are also quantitatively consistent with the XPS (Fig. 7) which showed some increase in the amount of iron carbide in the iron catalysts after the promotion.

The STEM-HAADF (High Angle Annular Dark Field) images and EDX (Energy Dispersive X-ray Spectroscopy) mapping data have provided the in-depth information about the interaction between iron and Bi and Pb promoters. The observed strong effects on the catalytic performance of Fe catalysts might be therefore due to the intimate contact between Fe and promoter due to higher mobility of promoters. The Bi and Pb promoters have low melting temperature (Bi 271 °C and Pb 327 °C) and the migration could therefore occur at the reaction temperature (350 °C). Fig. 13 shows STEM-HAADF image and EDX mapping of the FeBi/CNT catalyst prepared by co-impregnation and activated in CO. Interestingly, in the activated catalyst, the Bi promoter is located in close proximity to iron.

In order to provide further insights into the migration phenomena of the promoter, we prepared FeBi and FePb hybrid catalysts by mechanical mixing of Fe/CNT with Bi/CNT for 10 min in an agate mortar. The hybrid catalysts have the same Fe/Bi or Fe/Pb molar ratios as in the counterparts prepared by impregnation. Fig. 14 shows STEM-HAADF image and EDX mapping of the freshly mixed and calcined Fe/CNT + Bi/CNT catalysts. In the freshly calcined catalysts, the zones with higher Fe and Bi contents are clearly separately over the CNT support. Interestingly, Bi oxide species preferentially occupy the internal channels of CNT, while iron species are located both on the CNT outer surface and inside the CNT. Iron and bismuth distributions radically change after catalyst activation in carbon monoxide (Fig. 15). The images of the activated samples clearly show that most of the Bi particles are present in the surface of the iron and form a shell of promoter over the iron carbide core. Similar localization of the promoters at the interface of iron carbide nanoparticles was also observed in the spent catalysts after the reaction (Fig. 16). The particles inside the CNT tubes sinter to a lesser degree. This is consistent with previous works [49,57,58].

The characterization data are consistent with the catalytic results. The mixed catalysts also show high activity compared with the Fe/CNT catalysts (Table 3). Thus, we can conclude that Bi and Pb migrate to the surface of the iron during the reaction. This migration shows positive effect to the activity and selectivity.

To summarize, the following phenomena due to the promotion can positively affect the reaction rate and selectivity over the iron catalysts supported by CNT. First, a close contact between iron and promoters seems to enhance iron carbidisation in the promoted catalysts. This suggestion is consistent with the Mössbauer, in-situ magnetization and XPS data.

Second, the catalytic performance can be enhanced by facilitating CO dissociation on iron carbide via oxygen removal from iron carbide by scavenging with the promoters. Similar effects were previously [28] observed over the silica supported iron catalysts. The promoting elements located at the interface to iron carbide nanoparticles showed very easy changes of the oxidation state from metal to the oxide one in the presence of syngas. These changes attributed to the migration of oxygen atoms during carbon monoxide dissociation can lead to the partial oxidation of promoters. The oxidized promoters can be then

reduced by carbon monoxide with release of carbon dioxide molecules. The suggestion about facilitating of carbon oxide dissociation in the presence of promoters with scavenging of oxygen atoms is consistent with higher WGS reaction rates observed over the promoted catalysts. High CO_2 selectivity observed over the Bi and Pb-promoted catalysts after extrapolation to zero conversion indicates that CO_2 could be a primary reaction product over these catalysts.

The third effect occurring on the promotion is relevant to simultaneous slowing down secondary hydrogenation of olefins, reducing chain growth probability and C_{5+} hydrocarbon selectivity. The promoted catalysts display lower chain growth probability and higher olefin to paraffin ratio compared to the Fe/CNT reference catalysts in particular at lower reaction pressure. This leads to less significant decrease in light olefin selectivity with higher conversion at higher reaction pressure and higher olefin selectivity observed at low reaction pressure in comparison with the unpromoted CNT supported iron catalyst.

4. Conclusion

New efficient Bi and Pb-promoted CNT supported iron catalysts for the syngas direct conversion to lower olefins under mild reaction conditions were developed for light olefin synthesis from syngas. The promoted iron catalysts present higher FT reaction rate and higher selectivity to the C_2-C_4 olefins (55–60%) under atmospheric pressure compared to the unpromoted counterpart. The promotion effect of Bi and Pb on iron carbide has been reinforced by their migration during the catalyst activation, which leads to their preferential localization at the interface with iron carbide nanoparticles.

The promotion effect of Bi and Pb on the catalytic performance of CNT supported iron catalysts can be tentatively attributed to three phenomena: enhancement of iron carbidisation and reducibility, facilitation of carbon monoxide dissociation via scavenging of oxygen atoms by the promoters, slowing down secondary olefin hydrogenation and carbon chain growth.

Acknowledgement

References

[1] H.M.T. Galvis, J.H. Bitter, C.B. Khare, M. Ruitenbeek, A.I. Dugulan, K.P. de Jong, Science 335 (2012) 835–838.
[2] H.M.T. Galvis, A.C. Koeken, J.H. Bitter, T. Davidian, M. Ruitenbeek, A.I. Dugulan, K.P. de Jong, Catal. Today 215 (2013) 95–102.
[3] K. Cheng, B. Gu, X. Liu, J. Kang, Q. Zhang, Y. Wang, Angew. Chem. 128 (2016) 4803–4806.
[4] P. Tian, Y. Wei, M. Ye, Z. Liu, ACS Catal. 5 (2015) 1922–1938.
[5] S. Xu, A. Zheng, Y. Wei, J. Chen, J. Li, Y. Chu, M. Zhang, Q. Wang, Y. Zhou, J. Wang, F. Deng, Z. Liu, Angew. Chem. 52 (2013) 11564–11568.
[6] F. Jiao, J. Li, X. Pan, J. Xiao, H. Li, H. Ma, M. Wei, Y. Pan, Z. Zhou, M. Li, S. Miao, J. Li, Y. Zhu, D. Xiao, T. He, J. Yang, F. Qi, Q. Fu, X. Bao, Science 351 (2016) 1065–1068.
[7] K. Cheng, B. Gu, X. Liu, J. Kang, Q. Zhang, Y. Wang, Angew. Chem. 55 (2016) 4725–4728.
[8] K.P. de Jong, Science 351 (2016) 1030–1031.
[9] X. Chen, D. Deng, X. Pan, Y. Hu, X. Bao, Chem. Commun. 51 (2015) 217–220.
[10] M. Casavola, J. Hermannsdörfer, N. de Jonge, A.I. Dugulan, K.P. de Jong, Adv. Funct. Mat. 25 (2015) 5309–5319.
[11] M. Casavola, J. Xie, J.D. Meeldijk, N.A. Krans, A. Goryachev, J.P. Hofmann, A.I. Dugulan, K.P. de Jong, ACS Catal. 7 (2017) 5121–5128.
[12] B. Gu, S. He, W. Zhou, J. Kang, K. Cheng, Q. Zhang, Y. Wang, J. Energy Chem. 26 (2017) 608–615.
[13] E. de Smit, B.M. Weckhuysen, Chem. Soc. Rev. 37 (2008) 2758–2781.
[14] H.M. Torres Galvis, K.P. de Jong, ACS Catal. 3 (2013) 2130–2149.
[15] H.M.T. Galvis, A.C. Koeken, J.H. Bitter, T. Davidian, M. Ruitenbeek, A.I. Dugulan, K.P. de Jong, J. Catal. 303 (2013) 22–30.
[16] X. Duan, D. Wang, G. Qian, J.C. Walmsley, A. Holmen, D. Chen, X. Zhou, J. Energy Chem. 25 (2016) 311–317.
[17] F. Jiang, M. Zhang, B. Liu, Y. Xu, X. Liu, Catal. Sci. Tech. 7 (2017) 1245–1265.
[18] Y. Yuan, S. Huang, H. Wang, Y. Wang, J. Wang, J. Lv, Z. Li, X. Ma, ChemCatChem 9 (2017) 3144–3152.
[19] K. Cheng, V.V. Ordomsky, B. Legras, M. Virginie, S. Paul, Y. Wang, A.Y. Khodakov, Appl. Catal. A 502 (2015) 204–214.
[20] Z. Li, L. Zhong, F. Yu, Y. An, Y. Dai, Y. Yang, T. Lin, S. Li, H. Wang, P. Gao, Y. Sun, M. He, ACS Catal. 7 (2017) 3622–3631.
[21] P. Zhai, C. Xu, R. Gao, X. Liu, M. Li, W. Li, X. Fu, C. Jia, J. Xie, M. Zhao, X. Wang, Y.W. Li, Q. Zhang, X.-D. Wen, D. Ma, Angew. Chem. 55 (2016) 9902–9907.
[22] H. Wan, B. Wu, C. Zhang, H. Xiang, Y. Li, J. Molec, Catal. A 283 (2008) 33–42.
[23] Y. Liu, J.-F. Chen, J. Bao, Y. Zhang, ACS Catal. 5 (2015) 3905–3909.
[24] N. Lohitharn, J.G. Goodwin Jr., J. Catal. 260 (2008) 7–16.
[25] N. Lohitharn, J.G. Goodwin Jr, Catal. Commun. 10 (2009) 758–762.
[26] P. Munnik, P.E. de Jongh, K.P. de Jong, Chem. Rev. 115 (2015) 6687–6718.
[27] A.C. Koeken, T. Galvis, M. Hirsa, T. Davidian, M. Ruitenbeek, K.P. De Jong, Angew. Chem. 51 (2012) 7190–7193.
[28] V.V. Ordomsky, Y. Luo, B. Gu, A. Carvalho, P.A. Chernavskii, K. Cheng, A.Y. Khodakov, ACS Catal. 7 (2017) 6445–6452.
[29] G. Connell, J.A. Dumesic, J. Catal. 92 (1985) 17–24.
[30] A.N. Pour, Y. Zamani, A. Tavasoli, S.M. Kamali Shahri, S.A. Taheri, Fuel 87 (2008) 2004–2012.
[31] T. Li, Y. Yang, C. Zhang, X. An, H. Wan, Z. Tao, H. Xiang, Y. Li, F. Yi, B. Xu, Fuel 86 (2007) 921–928.
[32] A. Nakhaei Pour, S.M.K. Shahri, Y. Zamani, M. Irani, S. Tehrani, J. Nat. Gas Chem. 17 (2008) 242–248.
[33] X. Pan, Z. Fan, W. Chen, Y. Ding, H. Luo, X. Bao, Nat. Mater. 6 (2007) 507–511.
[34] J.-D. Xu, K.-T. Zhu, X.-F. Weng, W.-Z. Weng, C.-J. Huang, H.-L. Wan, Catal. Today 215 (2013) 86–94.
[35] J. Lu, L. Yang, B. Xu, Q. Wu, D. Zhang, S. Yuan, Y. Zhai, X. Wang, Y. Fan, Z. Hu, ACS Catal. 4 (2014) 613–621.
[36] R.M. Malek Abbaslou, J. Soltan, A.K. Dalai, Fuel 90 (2011) 1139–1144.
[37] P.A. Chernavskii, J.-A. Dalmon, N.S. Perov, A.Y. Khodakov, Oil Gas Sci. Techn. 64 (2009) 25–48.
[38] P.A. Chernavskii, A.Y. Khodakov, G.V. Pankina, J.-S. Girardon, E. Quinet, Appl. Catal. A 306 (2006) 108–119.
[39] M. Virginie, V.V. Ordomsky, C. Cordier, P.A. Chernavskii, M.I. Ivantsov, S. Paul, Y. Wang, A.Y. Khodakov, J. Catal. 328 (2015) 139–150.
[40] R.M.M. Abbaslou, A. Tavasoli, J. Soltan, A.K. Dalai, Appl. Catal. A 367 (2009) 47.
[41] K. Mai, T. Elder, L.H. Groom, J.J. Spivey, Catal. Commun. 65 (2015) 76–80.
[42] V. Subramanian, V.V. Ordomsky, B. Legras, K. Cheng, C. Cordier, P.A. Chernavskii, A.Y. Khodakov, Catal. Sci. Techn. 6 (2016) 4953–4961.
[43] G. Yu, B. Sun, Y. Pei, S. Xie, S. Yan, M. Qiao, K. Fan, X. Zhang, B. Zong, J. Am. Chem. Soc. 132 (2010) 935–937.
[44] C.P. Hunt, B.M. Moskowitz, S.K. Banerjee, Magnetic properties of rocks and minerals, Rock Physics & Phase Relations, American Geophysical Union, 2013, pp. 189–204.
[45] M.D. Shroff, D.S. Kalakkad, K.E. Coulter, S.D. Kohler, M.S. Harrington, N.B. Jackson, A.G. Sault, A.K. Datye, J. Catal. 156 (1995) 185–207.
[46] C. Yang, H. Zhao, Y. Hou, D. Ma, J. Am. Chem. Soc. 134 (2012) 15814–15821.
[47] C. Wang, C. Shao, Y. Liu, L. Zhang, Scripta Mater. 59 (2008) 332–335.
[48] C. Chang, L. Zhu, Y. Fu, X. Chu, Chem. Eng. J. 233 (2013) 305–314.
[49] J. Xiao, X. Pan, S. Guo, P. Ren, X. Bao, J. Am. Chem. Soc. 137 (2015) 477–482.
[50] G.P. Van Der Laan, A.A.C.M. Beenackers, Catal. Rev. – Sci. Eng. 41 (1999) 255–318.
[51] R.A. Dictor, A.T. Bell, J. Catal. 97 (1986) 121–136.
[52] B.H. Davis, Catal. Today 84 (2003) 83–98.
[53] M.E. Dry, Catal. Today 6 (1990) 183–206.
[54] M.E. Dry, Appl. Catal. A 138 (1996) 319–344.
[55] W. Ngantsoue-Hoc, Y. Zhang, R.J. O'Brien, M. Luo, B.H. Davis, Appl. Catal. A 236 (2002) 77–89.
[56] J.-Y. Park, Y.-J. Lee, P.K. Khanna, K.-W. Jun, J.W. Bae, Y.H. Kim, J. Molec. Catal. A 323 (2010) 84–90.
[57] W. Chen, Z. Fan, X. Pan, X. Bao, J. Am. Chem. Soc. (2008) 9414–9419.
[58] Z. Yang, X. Pan, J. Wang, X. Bao, Catal. Today 186 (2012) 121–127.